Impact of platinum group metals (Ru, Pd, Rh) on the dissolution of UO_2

Théo Cordara, Solène Bertolotto, Laurent Claparede, Stéphanie Szenknect, Adel Mesbah, Renaud Podor, Claire Lavalette, Nicolas Dacheux

PII: S0022-3115(19)30615-4

DOI: https://doi.org/10.1016/j.jnucmat.2019.151836

Reference: NUMA 151836

To appear in: *Journal of Nuclear Materials*

Received Date: 9 May 2019

Revised Date: 21 September 2019

Accepted Date: 3 October 2019

Please cite this article as: Thé. Cordara, Solè. Bertolotto, L. Claparede, Sté. Szenknect, A. Mesbah, R. Podor, C. Lavalette, N. Dacheux, Impact of platinum group metals (Ru, Pd, Rh) on the dissolution of UO_2, *Journal of Nuclear Materials* (2019), doi: https://doi.org/10.1016/j.jnucmat.2019.151836.

Impact of Platinum Group Metals (Ru, Pd, Rh) on the dissolution of UO_2

Théo Cordara[1,2], Solène Bertolotto[1], Laurent Claparede[1], Stéphanie Szenknect[1], Adel Mesbah[1], Renaud Podor[1], Claire Lavalette[3], Nicolas Dacheux[1 *]

[1] ICSM, CEA, CNRS, ENSCM, Univ Montpellier, Site de Marcoule, Bât. 426, BP 17171, 30207 Bagnols-sur-Cèze, France

[2] NucleUS Immobilisation Science Laboratory, Department of Materials Science and Engineering, Sir Robert Hadfield Building, S1 1JE, The University of Sheffield, UK

[3] ORANO NC, 1 place Jean Millier, 92084 La Défense, France

Corresponding author :

Prof. Nicolas Dacheux

ICSM, CEA, CNRS, ENSCM, Univ Montpellier
Site de Marcoule, Bât. 426
BP 17171, 30207 Bagnols-sur-Cèze
France

Phone : +33 466339205
Fax : +33 466797611
e-mail : nicolas.dacheux@umontpellier.fr

Highlights

Sintered UO_2 samples doped with PGM (Pd, Rh, Ru) have been dissolved in nitric acid solutions

Increase of the normalised dissolution rate and decrease of the duration of the induction period have been observed in the presence of PGM bearing ε metallic particles

Catalytic reaction involving nitrogen species formed close to the PGM bearing ε metallic particles has been suggested

No synergistic effect was evidenced when mixing the three PGM elements.

Abstract

The effect of metallic particles containing Platinum Group Metal (PGM) elements on the dissolution of sintered UO_2 samples was examined through the development of multiparametric dissolution tests on sintered UO_2 and UO_2 + 3 mol.% PGM samples. This effect was found to be more important for $C_{HNO_3} < 1$ mol.L^{-1} whereas it was lowered for higher nitric acid concentrations due to the preponderant oxidation of U(IV) by nitrate ions. Increase of the normalised dissolution rate of the ceramics was associated to the presence of PGM elements along with the decrease of the duration of the induction period (the stronger effect being observed for ruthenium). Simultaneously, the decrease of the apparent activation energy associated to the reaction of dissolution supported the existence of catalytic effect. This latter was connected to redox reaction between the metallic particles and nitrate ions either in solution or at the PGM/UO_2/solution interface. The involved reactions induced the formation of nitrogen species close to the PGM bearing particles. Among them, nitrous acid played an important role due to its strong oxidative power regarding to U(IV). Additionally, no synergistic effect was evidenced when mixing the three PGM elements.

1. Introduction

During its stay in nuclear reactor, the nuclear fuel is subjected to various phenomena such as neutron irradiation, thermal and/or mechanical constraints which can strongly affect several of its chemical, physico-chemical and microstructural properties of interest. Neutron irradiation leads to the formation of many new elements in the spent nuclear fuel (SNF), among which various fission products (FP). The oxygen set-aside SNF is composed of remaining uranium (about 96 wt. %), plutonium (1 wt. %), minor actinides (0.1 wt. %) and FP (3 – 4 wt.) representing about 40 elements. Kleykamp [1] and Ewing [2] classified the main fission products in four categories according to their behaviour in the SNF:

- Fission gases and other volatiles elements such as Kr, Xe, Ru, I, Cs and Te;
- FP forming metallic precipitates (usually named ε particles): i.e. Mo, Tc, Ru, Rh, Pd, Ag, Cd, In, Sn, Sb, Te and Se;
- FP present as oxide precipitates, including Rb, Sr, Zr, Nb, Mo, Se, Te, Cs and Ba;
- FP dissolved in the UO_2 matrix, which is partly the case for Ru, Sr, Y, Zr, Nb, fully for lanthanide (La, Ce, Pr, Nd, Pm, Sm, Eu) and actinide elements (U, Np, Pu, Am, Cm).

Thus, the composition of SNF is varying as a function of the operating conditions in the nuclear reactor [3]. Bruno *et al.* [3] mentioned that the amount of FP was gradually increasing as a function of the burn-up. Indeed, the oxygen/metal ratio [3], the initial composition within the fuel, the burn-up [4, 5], the radioactive decay as well as the thermal gradients in the fuel rods are affecting the rate of production, the distribution and the location of the FP in the SNF. Furthermore, some interactions can be observed between the main four categories of FP. For all these reasons, SNF appears as a very complex system considering either its chemical composition and its microstructure [2].

In several countries, SNF are reprocessed after their stay in the reactor with the aim to recycle uranium and plutonium prior the final disposal of radioactive waste. Thus, SNF dissolution constitutes the head-end step of the SNF reprocessing, this one being very complex due to the chemistry and microstructure of the SNF. This dissolution step is usually performed in concentrated nitric acid at about 90°C for several hours [5-16].

Current studies performed on the SNF durability are usually based on global elementary inventory in solution for various conditions. In this field, dissolution experiments were mainly realised in concentrated nitric acid solution for SNF reprocessing whereas leaching tests were usually conducted in aqueous solution close to neutrality or slightly alkaline for the long-term repository of SNF in underground repository site. However, these studies did not allow ranking the individual effect of the various SNF components during their dissolution [6-15, 17]. Furthermore, at the end of the dissolution step, dissolution slimes as residues are usually found in solution [5]. They are mainly composed of metallic inclusions found in the SNF, fragments of the nuclear fuel rods, refractory

materials or impurities in the nuclear fuels. Due to their incomplete dissolution, metallic particles could affect the reprocessing of these elements from SNF. So, it seems to be interesting to understand the role of these phases during the dissolution process and more particularly the impact of such metallic elements on the SNF dissolution kinetics and mechanisms. Ikeda et al. previously highlighted the acceleration effect of noble particles (Rh, Pd and Ru) incorporated in UO_2 on the dissolution in nitric acid solution. This effect was considered to be catalytic with direct interactions between UO_2 and noble particles [18].

Fission products found as metallic precipitates (ε particles) are mainly composed of molybdenum, ruthenium, palladium, rhodium and technetium representing 0.6 mol.% of the SNF [19]. Molybdenum is found in various forms because of a very complex speciation. Thus, in order to simplify the system, this element was not included in this study. PGM were incorporated to uranium dioxide according to the following distribution: Rh = 10 %; Pd = 36 %; Ru = 54%, which is representative of the composition of metallic particles in SNF [19]. Moreover, the amount of PGM added to UO_2 was increased from 0.6 mol.% (amount found in the SNF) to 3 mol.% in order to enhance the effect of such FP on the dissolution of UO_2. The multiparametric study associated to the kinetics of dissolution of UO_2 + 3 mol.% PGM pellets was performed in 0.1 to 4 mol.L^{-1} HNO_3 for temperatures ranging from 22 to 60°C. Dissolution results obtained in this work were finally compared to those compiled during the dissolution of UO_2 presented in previous work [20].

2. Experimental section

2.1. Preparation of uranium dioxide with PGM's pellets

Uranium dioxide samples doped with PGM samples were prepared by using wet chemistry route. Oxalate precipitation was first used in order to co-precipitate uranium and PGM. However, ICP-AES analyses proved that only very few amounts of PGM were precipitated in the final samples. For this reason, hydroxide precipitation was considered to allow quantitative precipitation [21]. This synthesis involved a mixture of concentrated uranium (IV) chloride solution (0.7 $mol.L^{-1}$, *i.e.* 1.8×10^{-2} mole of uranium) with PGM bearing solution. This latter was obtained by dissolution of hydrated ruthenium (III) chloride (Sigma Aldrich, 99.9 %), hydrated rhodium (III) chloride (Sigma Aldrich, 99.9 %) and palladium (II) chloride (Sigma Aldrich, 99.9 %) in 1 $mol.L^{-1}$ HCl. The concentrations of ruthenium, rhodium and palladium were measured in this solution by ICP-AES. The three elements were added to uranium dioxide with a global content of 3 mol.% and the following distribution: Rh (10 %) - Pd (36 %) and Ru (54%) to mimic the composition of the metallic precipitates in SNF. Then, the solution was mixed with a large excess of ammonium hydroxide (400%) at room temperature, leading to the instantaneous precipitation of the elements. The precipitate was stirred for 30 minutes in air. The freshly prepared precipitates were washed twice with water and once with ethanol in order to remove all traces of ammonium hydroxide. After this washing step, the hydroxide fine powders were introduced into a flask with 50 mL of ethanol and then placed under vacuum to be finally stirred mechanically at 40°C. After the complete evaporation of the solvent, the stirring was maintained for a few minutes then the flask was filled with nitrogen in order to avoid the oxidation of uranium (IV) into uranyl. For the same reason, the resulting powdered sample was further stored under inert atmosphere. It was finally converted to oxide by heating at 800°C during 4 hours under reducing atmosphere (Ar + 5% H_2). This protocol allowed the elimination of water and carbon contained in the sample, as already described by Martinez *et al.* [21].

Dense pellets of uranium dioxide doped with PGM were prepared through sintering step. First, the oxide powder was ball milled (30 minutes, 30 Hz) in zirconia jar using a MM 400 Retzsch mixer mill. Milled powder was pressed uniaxially at 500 MPa using a tri-shells die of 5 mm in diameter. 1 to 2 mm thick green pellets were obtained with a densification rate of about 50 %. These green pellets (150 to 200 mg) were sintered during 8 hours at 1500°C under reducing atmosphere (Ar + 5% H_2) to finally prepare well densified pellets (≈ 90 % of theoretical density).

2.2. Characterisation of the samples

The stoichiometry of each prepared samples was determined by ICP-AES after the full dissolution of an aliquot of the powder in 2 $mol.L^{-1}$ HNO_3 and direct analyses of the supernatants collected during all the washing steps. Depending on the solution considered, *i.e.* on the basis of the

uranium concentration, the aliquots were diluted with 0.2 mol.L^{-1} HNO_3. Then, uranium and PGM concentrations were determined using inductively-coupled plasma atomic emission spectroscopy (ICP-AES, Spectro Arcos). The analysis was performed considering the results obtained at λ = 279.394 and 329.133 nm for uranium, at λ = 240.272 and 267.876 nm for ruthenium, at λ = 252.053 and 249.077 nm for rhodium and at λ = 324.270 and 229.651 nm for palladium. ICP-AES analyses were calibrated by using several uranium and PGM standard solutions prepared by dilution of certified 1000 ppm standard solutions. The elemental concentrations were determined in solution from three replicates. Otherwise, ICP-AES showed an increase of the PGM detection limit in the presence of uranium. Indeed, the PGM detection limits obtained for this analytical protocol were 10^{-1} ppm and 10^{-2} ppm in the presence and in the absence of uranium in the solution, respectively. This effect was explained by interferences coming from the higher amount of uranium solubilized compared to PGM (due to the composition of the sample).

The characterization of the prepared samples was carried out by PXRD using a Bruker D8-Advance Diffractometer (LynxEye detector) in the reflexion geometry with the Cu-Kα1,2 radiation (λ = 1.5418 Å). The data were collected at room temperature with an angular range of 5° < 2θ < 100°, a step of 0.0167° and a total counting time of about 170 minutes corresponding to 1.77s per step. All the PXRD patterns were refined by the Rietveld method using the Cox–Hastings pseudo-Voigt profile function implemented in the Fullprof suite program [22]. During all the refinements, the conventional profile/structure parameters (zero shift, unit cell parameters, scale factors, global thermal displacement and asymmetric parameters) were allowed to vary. Moreover, for each phase, the modelling of the intrinsic microstructure parameters was performed by applying an anisotropic size model.

The densification rates were determined by geometric measurements thanks to a calliper splint and by ethanol pycnometry. From geometrical measurements, the apparent density, d_{geo} (g.cm^{-3}) was evaluated and compared to the calculated density of UO_2 ($d_{calc.}$ = 10.97 g.cm^{-3}), leading to the determination of the total porosity. Ethanol pycnometry was also performed to determine the closed porosity. The relative uncertainties associated to apparent and pycnometric densities reached 1 % and 2 %, respectively. The total porosity (P_{tot} , expressed in %), the closed porosity (P_{closed}, expressed in %) and the open porosity (P_{open}, expressed in %) were thus determined according to the three following equations:

$$P_{tot} = \left(1 - \frac{d_{geo}}{d_{calc}}\right) \times 100 \quad (1)$$

$$P_{closed} = \left(1 - \frac{d_{pycno}}{d_{calc}}\right) \times 100 \quad (2)$$

$$P_{open} = P_{tot} - P_{closed} \quad (3)$$

The morphology of the samples was studied by SEM with a FEI Quanta 200 environmental scanning electron microscope using backscattered electron detector (BSED) or secondary electron detector (SE) in vacuum conditions with an acceleration voltage of 25 kV. The samples were always directly analysed without any additional preparation step such as metallization.

SEM micrographs recorded at low magnification were used to determine the grain size distribution at the surface of UO_2 dense pellets using the FiJi software and a touchscreen. Each grain was circled on a representative SEM micrograph then the area and diameter of the grains were evaluated with the help of the "analyse particles" plugin implemented in the FiJi software. Almost 200 grains were analyzed in order to evaluate the grain size distribution and associated statistics. They were also used to evaluate the initial specific surface area (S_{SA}, expressed in $m^2.g^{-1}$) of the pellets using the SESAM (Study of Evolving Surface Area by Microscopy) method [23, 24]. In this field, 5 images of 92 µm × 62 µm were binarized using the FiJi software to determine the surface area of the pores observed in the investigated domains. The pore diameter distribution was evaluated from these images using the "analyse particles" plugin. Then, the surface area associated to the pores was obtained assuming that the pore size distribution of the analysed domain was representative of the whole sample and that the pores were cylindrical. Moreover, the depth of the pores was determined in order to respect the global open porosity developed by all the open pores and obtained from helium pycnometry (P_{open}). Then, the resulting surface was divided by the mass of the sample in order to calculate the specific surface area. For each sample, an average value of the specific surface area was deduced from the analysis of the 5 images recorded at low magnification.

2.3. Dissolution experiments

All the dissolution tests were performed in static conditions using polytetrafluoroethylene containers placed in oven at 40°C and 60°C or at room temperature. For such experiments, the pellets of 150 to 200 mg were put in contact with 25 mL of 0.1, 0.5, 1, 2 or 4 $mol.L^{-1}$ HNO_3 for few hours to several months. During this time, aliquots of 5 mL were regularly taken off and replaced by the same volume of fresh HNO_3 solution to maintain a constant volume of solution. These aliquots were analysed by ICP-AES in order to determine each elemental concentration in solution using the same conditions than that previously described. Moreover, complementary experiments were performed by using UO_2 sintered samples doped with one of the three PGM elements and by making dissolution tests with addition of PGM metallic particles in the solution.

The contribution associated to the presence of PGM metallic particles in solution was first followed during dissolution tests of UO_2 sintered samples. In order to compare these results with those obtained on UO_2 + 3 mol.% PGM sintered samples, a mass of metallic PGM particles was added to the solution in order to reach 3 mol.% PGM compared to the amount of uranium in the UO_2 pellet. A schematic view of this kind of experiments is presented in **Figure 1**. All the powders used were

commercial powders of PGM as metallic particles bought to STREM CHEMICALS with different purity grades: rhodium 99.8 %, ruthenium 99.9 % and palladium 99.95 %. In order to avoid any direct contact between UO_2 and PGM metallic particles, the pellet was put on a tripod within the dissolution device.

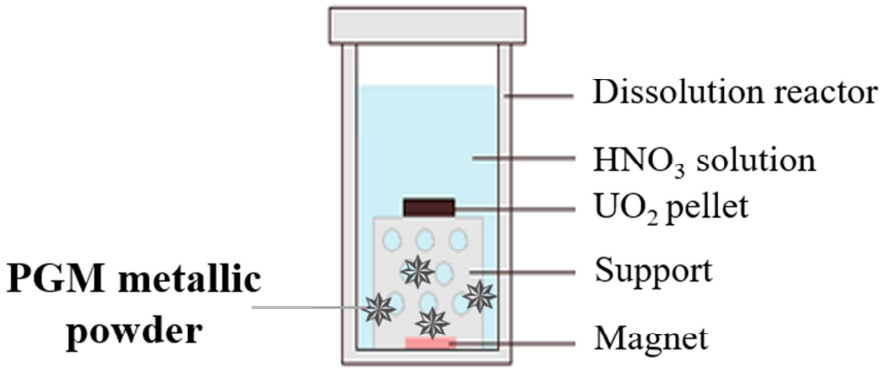

Figure 1. Schematic representation of the dissolution setup used during dissolution tests of UO_2 in the presence of PGM metallic particles in solution.

2.3.1. Definitions and normalisation

The mass of dissolved material at time *t*, $\Delta m(t)$ (in wt. %) was calculated as follows:

$$\Delta m(t) = \frac{m_i(t)}{f_i \times m(t=0)} \times 100 = \frac{C_i(t) \times V}{f_i \times m(t=0)} \times 100 \quad (4)$$

where $m_i(t)$ (g) corresponds to the total amount of the element *i* released in the solution at time *t* calculated from the elementary concentration, $C_i(t)$ (g.L^{-1}), and the volume of solution in contact with the solid, *V* (L). In this expression, f_i (g.g^{-1}) is the mass fraction of the element *i* in the solid and $m(t = 0)$ is the initial mass of the pellet (g).

According to literature, the normalised weight losses, $N_L(i)$ (g.m^{-2}) were calculated from the elemental concentrations as follows :

$$N_L(i,t) = \frac{m_i(t)}{f_i \times S(t)} = \frac{m_i(t)}{f_i \times S_{SA} \times \left(m(t=0) - \frac{m_i(t-1)}{f_i}\right)} \quad (5)$$

where $S(t)$ (m²) is the surface area of solid in contact with the solution at time *t*. It is worth noting that f_i and S_{SA} (m².g^{-1}) are considered to remain constant in equation (5).

The normalised dissolution rates, $R_L(i,t)$ (g.m^{-2}.d^{-1}), were derived from normalised weight losses following :

$$R_L(i,t) = \frac{d\,N_L(i,t)}{d\,t} \quad (6)$$

2.3.2. Impact of temperature and nitric acid concentration on the $R_{L,0}$ values

The multiparametric description of the kinetics of dissolution was proposed by Lasaga [25] based on experimental results. A general form of the rate law is given by:

$$R_L = k_0 \times e^{-E_{app}/RT} \times (\mathrm{H}^+)^{n_H} \times g(I) \times \prod_j (E_j)^{n_j} \times f(\Delta_R G) \quad (7)$$

where k_0 (g.m^{-2}.h^{-1}) is the rate constant, E_{app} (kJ.mol^{-1}) is the apparent activation energy of the overall reaction, R is the gas constant, T is the absolute temperature. (E_j) and (H^+) are the activities in the solution of E_j and H^+ species, respectively. n_H and n_j are the partial orders of the reaction related to the proton and to the species E_j, respectively. $g(I)$ indicates a possible dependence of the overall rate on the ionic strength, I in addition to that entering through the species activities. $f(\Delta_R G)$ accounts for the variation of the overall rate with the deviation from equilibrium of the solution. Keeping constant all the parameters except temperature, the dependence of the dissolution rate on temperature can thus be typically expressed using the Arrhenius law:

$$R_{L,0} = k'' \times \mathrm{e}^{-E_{app}/RT} \quad (8)$$

where k'' (g.m^{-2}.d^{-1}) is the apparent normalised rate constant of the dissolution reaction, independent of the temperature, but dependent on pH, ionic strength and composition of the dissolution medium and E_{app} (kJ.mol^{-1}) is the apparent activation energy of the overall reaction. E_{app} is usually determined from the variation of ln ($R_{L,0}$) versus the reciprocal of temperature. It is considered as a good indicator of the nature of predominant reaction driving the kinetics of the global dissolution mechanism. Typically, a dissolution mechanism kinetically limited by transport step is associated to an apparent activation energy lower than 20 kJ.mol^{-1}. When surface-controlled reactions are rate determining steps, E_{app} values are usually ranging from 40 to 80 kJ.mol^{-1}. This apparent activation energy is lower than that associated to the breaking of covalent bonds in crystals, which ranges between 160 and 400 kJ.mol^{-1} [26].

3. Results and discussion

3.1. Characterisation of the oxide powders

Results of ICP-AES analyses obtained on successive supernatants (coming from synthesis and washing steps) as well as from full dissolution of the prepared materials are gathered in **Table 1**. They showed the efficient and quantitative coprecipitation of uranium and PGM elements via the hydroxide route precipitation. Indeed, for each element considered, the obtained molar fraction was in good agreement with that expected. The prepared samples were thus composed of 97 mol.% of uranium and 3 mol.% of PGM (i.e. 1.6 mol.% of Rh, 0.3 mol.% of Pd, 1.1 mol.% of Ru) and will be noted thereafter UO_2 + 3 mol.% PGM.

Table 1. Expected and measured molar fractions of uranium and of each PGM of interest.

Elements	Expected molar fraction	Obtained molar fraction
U	0.97	0.97 ± 0.06
PGM	0.03	0.03 ± 0.02
Rh	0.016	0.016 ± 0.003
Pd	0.003	0.003 ± 0.001
Ru	0.011	0.011 ± 0.002

The SEM characterisation of UO_2 doped with PGM powder is presented in **Figure 2A**. It showed that the powder prepared from hydroxide to oxide conversion did not exhibit a well-defined morphology. Indeed, the powder was composed of nanometric particles as already observed by Martinez *et al.* [21] by TEM. According to the results reported by Martinez *et al.* [21] during the conversion of uranium-cerium oxide based materials, heating treatment at 800°C during 4 hours was used in order to guarantee the full conversion of the hydroxide precursors to the final oxides.

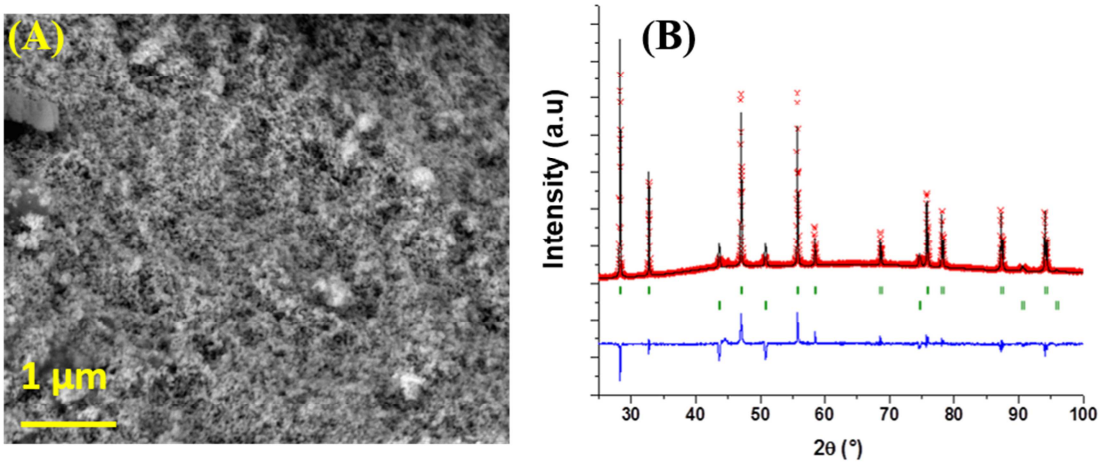

Figure 2. SEM micrograph of the as-prepared UO_2 + 3 mol.% PGM powder (A) and XRD pattern of UO_2 + 3 mol.% PGM recorded after conversion of uranium (IV) hydroxide precursor performed at 800°C during 4 hours under reducing atmosphere (B).

The XRD pattern of the prepared UO_2 doped with PGM (**Figure 2B**) was refined by the Rietveld method considering the fluorite type structure (Fm3m space group). The obtained unit cell parameter, a = 5.470 ± 0.001 Å, was in very good agreement with that reported for nearly stoichiometric UO_2 (a = 5.468 ± 0.001 Å [27], which shows that the PGM elements were not incorporated in the UO_2 fluorite-type structure. This observation was not surprising based on the characterization of SNF in which PGM elements are forming micrometric metallic particles.

3.2. Characterisations of the sintered pellets

The microstructural properties of the dense pellets of UO_2 + 3 mol.% PGM were characterized through geometric and pycnometric measurements and by SEM observations (**Table 2**). The specific surface area value was determined via the SESAM method thanks to SEM micrographs recorded at low magnification. It was calculated for each pellet used during the dissolution test. As this value corresponds to the observed porosity, it was taken into account for the determination of the dissolution rates through the normalization of the weight losses by the corresponding initial specific surface area.

Table 2. Example of densification rates obtained for one of the sintered pellets used during the dissolution experiments determined by geometric and pycnometric measurements ($\frac{d_{geo}}{d_{calc}}$ and $\frac{d_{pycno}}{d_{calc}}$, expressed in %), closed porosity and open porosity values (expressed in %) and specific surface area (expressed in $m^2.g^{-1}$) determined by the SESAM method. The uncertainties correspond to twice the standard deviation calculated for five measurements.

Sample	m_0 (g)*	d_{geo}/d_{calc} (%)	d_{pycno}/d_{calc} (%)	Closed porosity (%)	Open porosity (%)	Specific surface area ($m^2.g^{-1}$)
UO_2 + PGM	0.199	89 ± 1	93 ± 1	7 ± 2	4 ± 1	$(1.4 \pm 0.6) \times 10^{-2}$

* associated uncertainty of ± 0.001 g

SEM micrographs of sintered pellets of UO_2 + 3 mol.% PGM (**Figure 3A**) clearly showed the formation of white particles mainly located at the grain boundaries (at the surface and in the bulk) after the sintering step performed during 8 hours at 1500°C under reducing atmosphere (Ar + 5% H_2). These metallic particles are usually called “white particles” because of their characteristic contrast compared to the UO_2 observed by SEM using a secondary electron detector. They correspond to metallic alloys composed of PGM elements (Ru, Rh, Pd). X-EDS analyses confirmed that the chemical composition of these bi- or tri-metallic alloys particles was varying in the particles. Furthermore, no significant amount of PGM elements was found in the UO_2 matrix. Such microstructure reminded that was observed for SNF (**Figure 3B**) [28]. However, the average grain size of UO_2 in SNF was larger than that found in the synthesized samples. It was mainly assigned to the difference in the sintering temperatures of SNF (1740°C) and synthesized pellets (1550°C), which is favourable to the grain coarsening. The same observation was performed regarding the size of metallic particles (≈ 500 nm in SNF and < 100 nm in the as-prepared sintered materials).

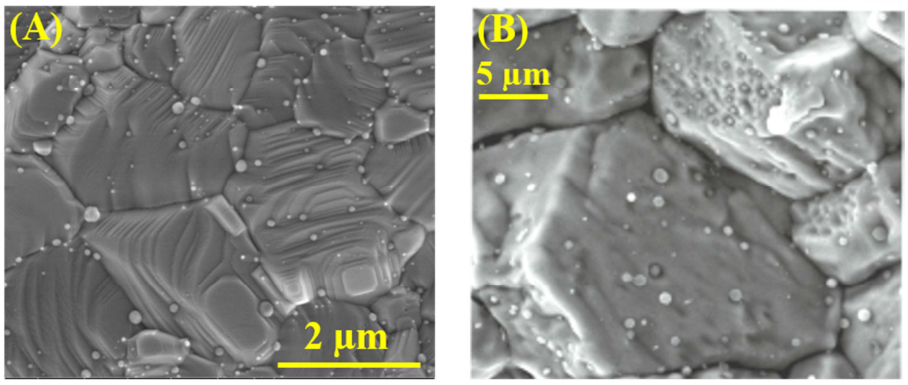

Figure 3. SEM micrographs of synthesized pellets of UO_2 + 3 mol.% PGM (A) and of SNF (B) [24].

One of the SEM micrographs recorded for sintered pellet of UO_2 + 3 mol.% PGM, representative of the surface is presented in **Figure 4A**. At least five images of 92 µm × 62 µm were used for each pellet in order to determine its specific surface area by the SESAM method. The analysis of the images performed with the FiJi software was also used to determine the grain size distribution (**Figure 4B**). Such distribution was representative for the various pellets prepared. The average grain size reached 0.6 ± 0.4 µm, which was lower than that reported by Martinez *et al.* using the hydroxide route for UO_2 (≈ 5 µm) [21]. This difference was surely due to the presence of PGM element in the sample, which could limit the grain growth.

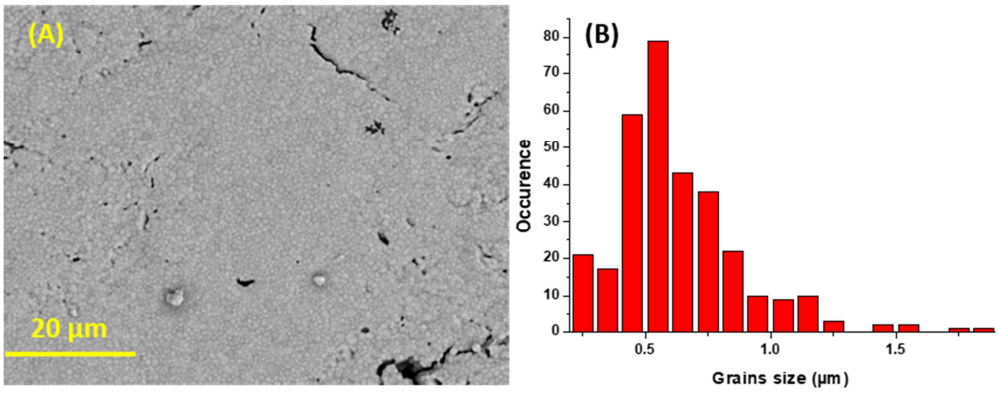

Figure 4. SEM micrograph of sintered pellet of UO_2 + 3 mol.% PGM recorded at low magnification (A) and estimated grain size distribution (B).

In order to better understand the impact of individual PGM particles (i.e. not mixed) during the dissolution of UO_2, several samples incorporating one of the PGM elements were prepared by hydroxide route then shaping with the same conditions than that already described in terms of milling, shaping and sintering. The results of characterization are summarized in **Table 3**. They showed that the pellets were dense and developed an initial specific surface area close to 5×10^{-2} $m^2.g^{-1}$. PGM

elements were found as metallic particles not only at the surface of the pellet but also in the bulk material, which was in agreement with the results obtained by incorporating simultaneously the three PGM.

Table 3. Densification rates of sintered pellets of UO_2 + 3 mol.% Ru, UO_2 + 3 mol.% Rh, UO_2 + 3 mol.% Pd used during dissolution tests, closed porosity and open porosity values, and specific surface area determined using the SESAM method. The uncertainties correspond to twice the standard deviation calculated from five measurements.

Sample	m (t = 0) (g) ± 0.001	Geometric densification rate (%)	Pycnometric densification rate (%)	Closed porosity (%)	Open porosity (%)	Specific surface area ($m^2.g^{-1}$)
UO_2 + 3 mol.% Rh	0.186	93 ± 1	94 ± 1	6 ± 1	1 ± 1	$(3.2 \pm 2.5) \times 10^{-2}$
UO_2 + 3 mol.% Ru	0.147	93 ± 1	95 ± 1	5 ± 1	2 ± 1	$(4.5 \pm 3.5) \times 10^{-2}$
UO_2 + 3 mol.% Pd	0.181	89 ± 1	92 ± 1	8 ± 1	3 ± 1	$(5.1 \pm 1.5) \times 10^{-2}$
UO_2 + 3 mol.% PGM *	0.199	89 ± 1	93 ± 1	7 ± 1	4 ± 1	$(1.4 \pm 0.6) \times 10^{-2}$

* UO_2 + 3 mol.% PGM is given as reference

3.3. Dissolution tests

3.3.1. Dissolution of sintered pellets of UO_2 + 3 mol.% PGM

In order to underline the influence of nitric acid concentration and temperature on the evolution of the normalised weight loss, $N_L(U)$ ($g.m^{-2}$), various dissolutions tests of UO_2 + 3 mol.% PGM sintered pellets were performed in static conditions with various nitric acid concentrations (0.1, 0.5, 1, 2 and 4 $mol.L^{-1}$) and temperatures (22, 40 and 60°C). The evolutions of the normalised weight losses and of the associated mass losses obtained at 22°C, 40°C and 60°C are reported in **Figure 5**, in **Figure 6** and in **Figure 7**, respectively. For several operating conditions, the normalised dissolution rates determined from the released PGM elements were not obtained with a good accuracy because of the very low concentrations of dissolved PGM elements compared to the detection limit of ICP-AES. This could be partly due to the very low solubility of the metallic particles containing ruthenium, rhodium and palladium in the conditions of the dissolution tests. Furthermore, as already mentioned, the limit of detection of these PGM elements was increasing in the presence of uranium.

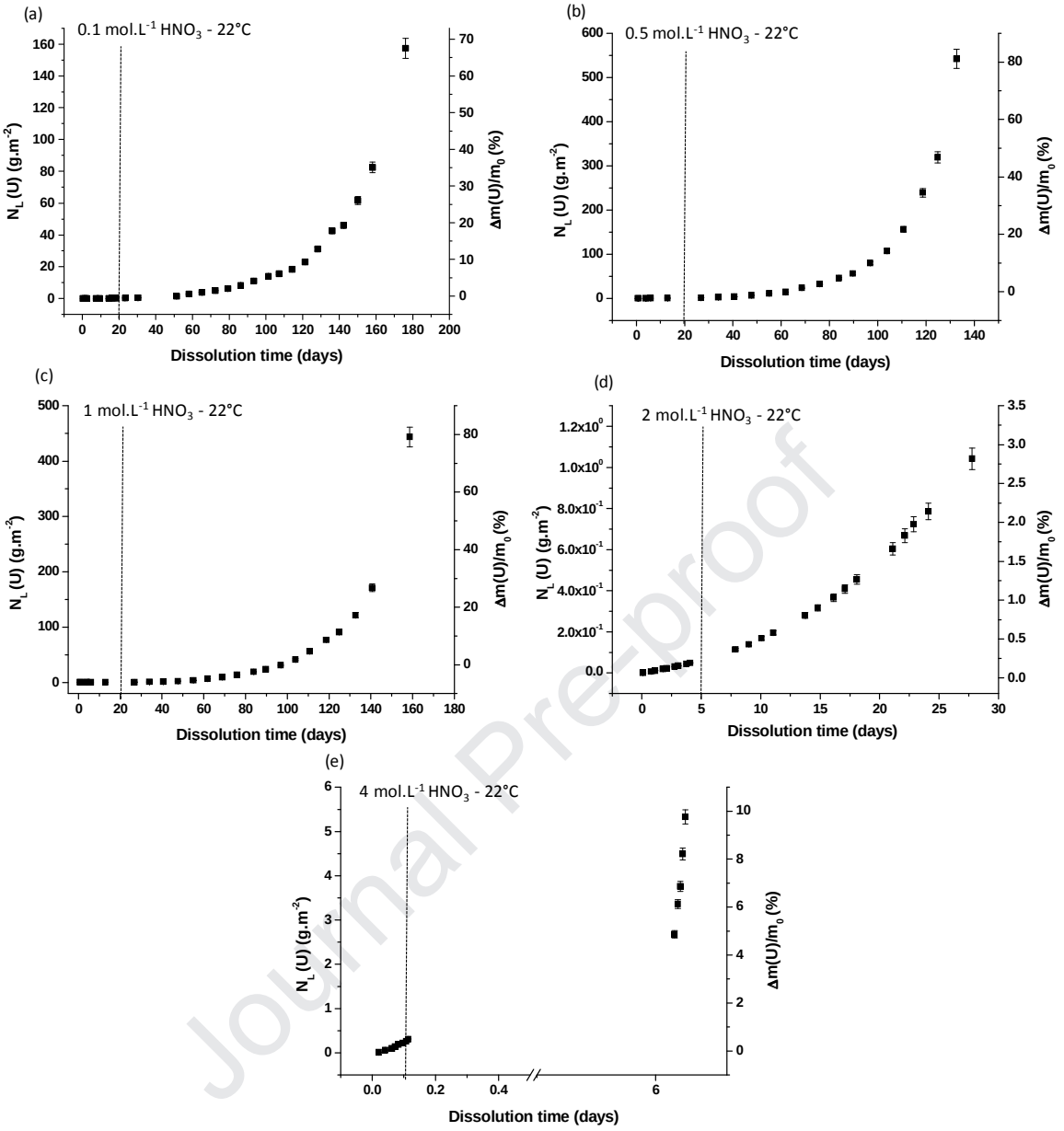

Figure 5. Evolution of the normalised weight losses N_L(U) (left vertical axis) and of associated relative mass losses $\Delta m(U)/m_0$ (right vertical axis) obtained during the dissolution of UO_2 + 3 mol.% PGM sintered pellets at 22°C and for various HNO_3 solutions: 0.1 mol.L^{-1} (a), 0.5 mol.L^{-1} (b), 1 mol.L^{-1} (c), 2 mol.L^{-1} (d) and 4 mol.L^{-1} (e). Dash lines point out the transition from step 2 (induction period) to step 3 (catalyzed domain) when evidenced.

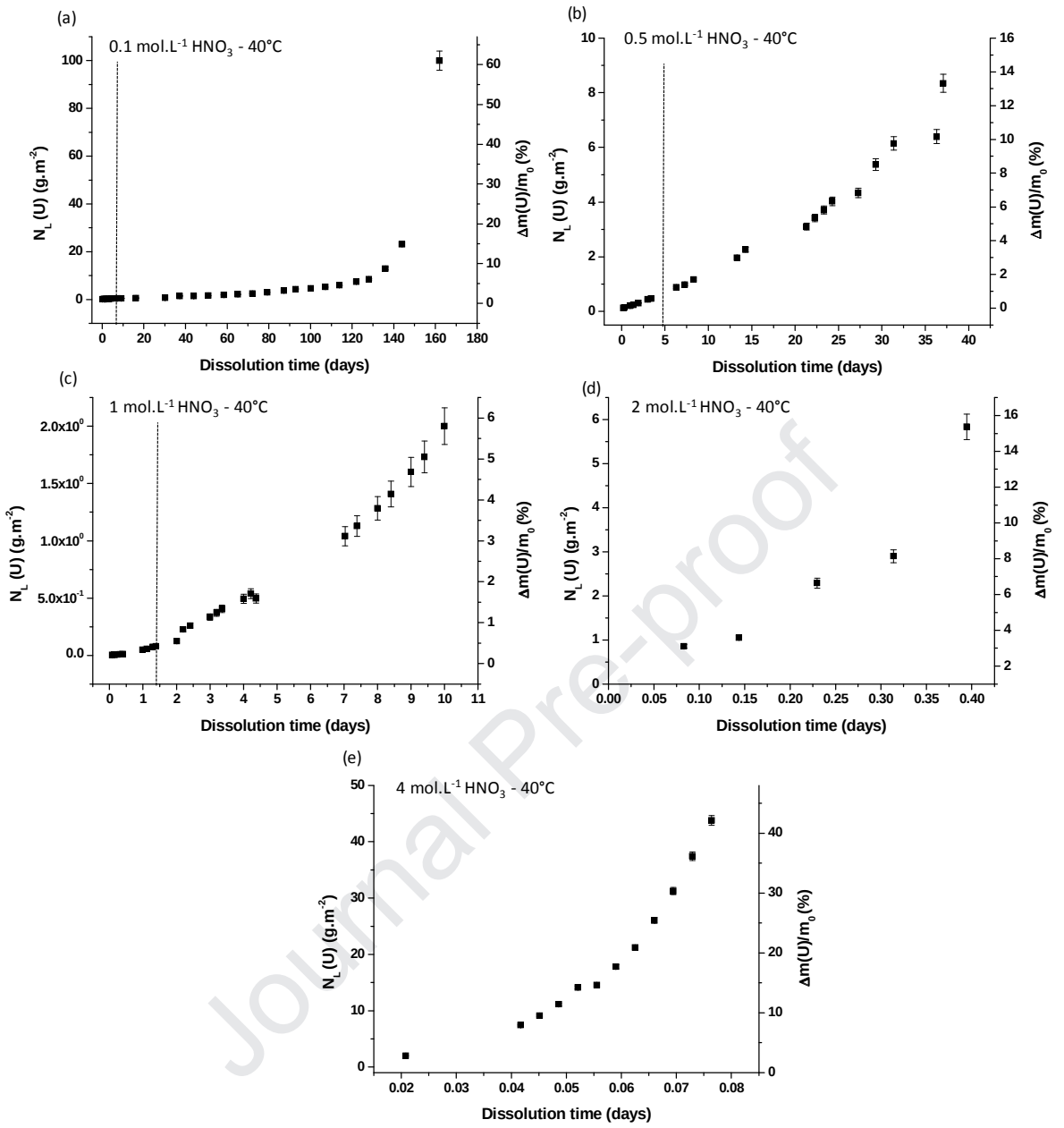

Figure 6. Evolution of the normalised weight losses N_L(U) (left vertical axis) and of associated relative mass losses $\Delta m(U)/m_0$ (right vertical axis) obtained during the dissolution of UO_2 + 3 mol.% PGM sintered pellets at 40°C and for various HNO_3 solutions: 0.1 mol.L^{-1} (a), 0.5 mol.L^{-1} (b), 1 mol.L^{-1} (c), 2 mol.L^{-1} (d) and 4 mol.L^{-1} (e). Dash lines point out the transition from step 2 (induction period) to step 3 (catalyzed domain) when evidenced.

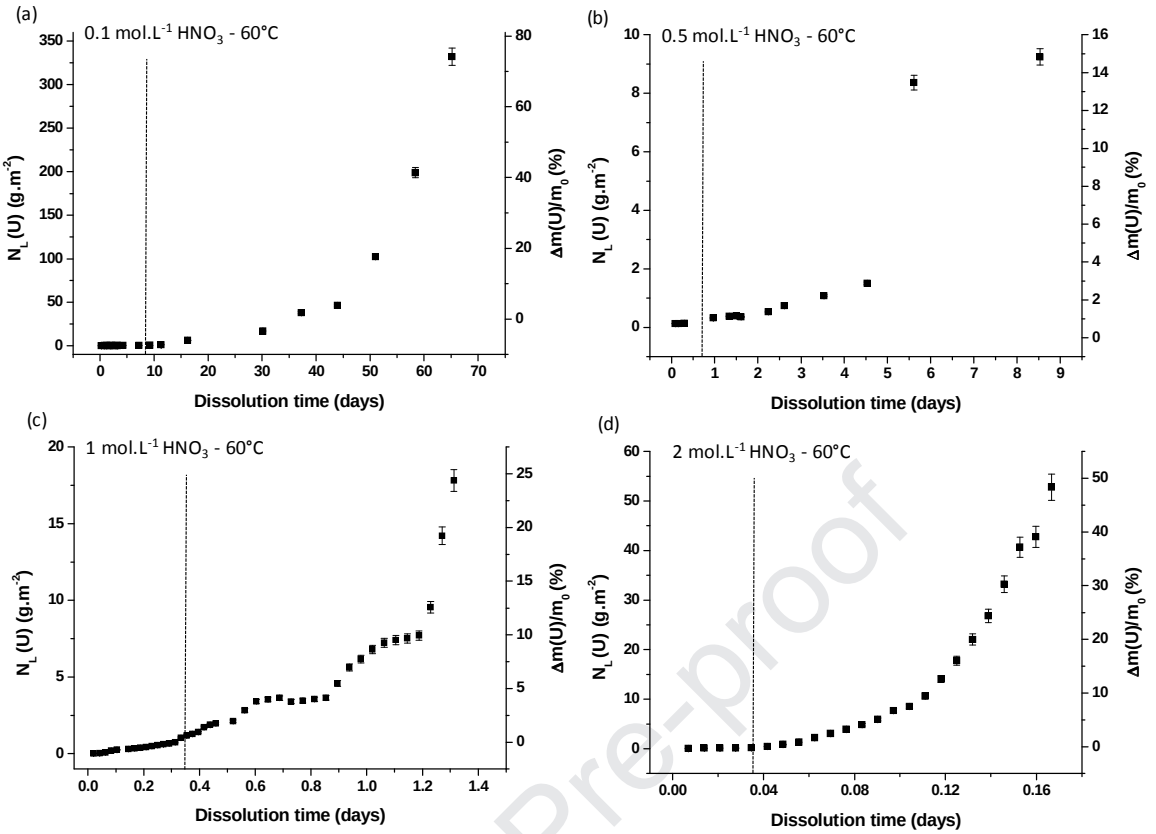

Figure 7. Evolution of the normalised weight losses N_L(U) (left vertical axis) and of associated relative mass losses $\Delta m(U)/m_0$ (right vertical axis) obtained during the dissolution of UO_2 + 3 mol.% PGM sintered pellets at 60°C and for various HNO_3 solutions: 0.1 mol.L^{-1} (a), 0.5 mol.L^{-1} (b), 1 mol.L^{-1} (c) and 2 mol.L^{-1} (d). Dash lines point out the transition from step 2 (induction period) to step 3 (catalyzed domain) when evidenced.

The comparison of the curves obtained regarding the evolutions of N_L (U) presented in **Figure 5-7** underlined shape modifications depending on the dissolution conditions considered. Cordara *et al.* [20] already demonstrated such shape variations when performing the dissolution of pure UO_2 pellets in the same conditions. They mentioned the existence of three dissolution steps as a function of the mass losses $\Delta m(U)/m_0$ (%).

In this study, two of these three steps were clearly observed in **Figures 5-7**. On the contrary, the first kinetics regime usually associated to defects and small amounts of over-stoichiometric uranium dioxide at the extreme surface, always evidenced for the lowest HNO_3 concentrations and temperatures (leading to uranium releases lower than 0.05 wt.%), was never observed during the dissolution of UO_2 + 3 mol.% PGM sintered pellets. According to the general trend presented in this study [20], the systematic absence of this "pulse" was due to higher initial uranium releases in the presence of PGM elements compared to pure UO_2 samples.

The second step called induction period was observed for each dissolution test. It was considered as a steady state, characterized by the linear evolution of the dissolved mass and of the

normalised weight loss and was associated to limited variation of the reactive surface area. All the normalized dissolution rate, $R_{L,0}$ ($g.m^{-2}.d^{-1}$), were determined in this domain from these linear evolutions. This step was maintained until the amount of uranium released remained lower than 1 wt.%. All the normalised dissolution rates, $R_{L,0}$(U) determined during this induction period are summarized in **Table 4** for each temperature and HNO_3 concentration. The dissolved relative mass, $\Delta m/m_0$ (expressed in wt. %) as well as the uranium concentration in solution, C_U ($mol.L^{-1}$) measured at the end of this induction period are also summarized for each condition.

During the induction period, the concentration of autocatalytic species progressively increase in the solution. When a sufficient concentration of autocatalytic species was reached in solution, the reaction rate increased due to the production of autocatalytic species with a higher rate (catalysed domain), leading to the end of the induction period. Consequently, the resulting dissolution rate increased non-linearly with time. This non-linearity was also due to the significant increase of the reactive surface area of the pellet in contact with the solution [20]. The transition from the induction period to the catalysed domain is pointed out by dash lines, when observed, in **Figures 5-7**.

Table 4. Normalised dissolution rates $R_{L,0}$(U) ($g.m^{-2}.d^{-1}$) determined during the steady state period during the dissolution of UO_2 + 3 mol.% PGM samples performed in various conditions (temperature, HNO_3 concentrations). $\Delta m/m_0$ (expressed in wt. %), associated duration of the steady state period (expressed in days) and uranium concentrations C_U ($mol.L^{-1}$) obtained at the end of the induction period.

HNO_3 concentration	**0.1 M**	**0.5 M**	**1 M**	**2 M**	**4 M**
22°C					
$R_{L,0}$(U) ($g.m^{-2}.d^{-1}$)	**$(1.2 \pm 0.2) \times 10^{-2}$**	**$(2.7 \pm 0.1) \times 10^{-2}$**	**$(1.6 \pm 0.1) \times 10^{-2}$**	**$(1.2 \pm 0.1) \times 10^{-2}$**	**2.9 ± 0.2**
End of steady state					
$\Delta m/m_0$ (wt. %)	0.4 – 0.6	0.8 – 2.4	0.4 – 1.1	0.2 – 0.4	0.4 – 0.6
Duration (days)	18 – 22	13 – 27	13 – 27	4.1 – 7.9	0.09 – 0.11
C_U ($mol.L^{-1}$)	$(1.2 – 1.7) \times 10^{-4}$	$(1.9 – 5.3) \times 10^{-4}$	$(1.1 – 2.9) \times 10^{-4}$	$(4.1 – 9.6) \times 10^{-5}$	$(1.3 – 1.8) \times 10^{-4}$
40°C					
$R_{L,0}$(U) ($g.m^{-2}.d^{-1}$)	**$(4.4 \pm 0.1) \times 10^{-2}$**	**$(1.1 \pm 0.1) \times 10^{-1}$**	**$(6.5 \pm 0.2) \times 10^{-2}$**	N.D.	N.D.
End of steady state					
$\Delta m/m_0$ (wt. %)	0.5 – 0.7	0.9 – 1.7	0.3 – 0.4	< 2.60	< 3.80
Duration (days)	4 – 7	3 – 6	1 – 2	< 0.08	< 0.02
C_U ($mol.L^{-1}$)	$(1.3 – 2.0) \times 10^{-4}$	$(2.9 - 5.3) \times 10^{-4}$	$(0.68 – 1.1) \times 10^{-4}$	$< 7.0 \times 10^{-4}$	$< 1.1 \times 10^{-3}$
60°C					
$R_{L,0}$(U) ($g.m^{-2}.d^{-1}$)	**$(6.2 \pm 0.3) \times 10^{-2}$**	**$(1.6 \pm 0.1) \times 10^{-1}$**	**2.4 ± 0.1**	**3.9 ± 1.0**	N.D.
End of steady state					
$\Delta m/m_0$ (wt. %)	0.8 – 1.3	0.3 – 0.7	1.4 – 3.0	0.4 – 0.9	N.D.
Duration (days)	7 – 9	0.3 – 1.0	0.3 – 0.4	0.03 – 0.04	N.D.
C_U ($mol.L^{-1}$)	$(2.3 – 3.6) \times 10^{-4}$	$(1.1 – 2.4) \times 10^{-4}$	$(4.0 – 5.7) \times 10^{-4}$	$(1.1 – 2.6) \times 10^{-4}$	N.D.

The results gathered in **Table 4** showed that the duration of the steady state was always decreasing when increasing the nitric acid concentration, which agrees well with the data obtained on pure UO_2 [20]. During this period, the concentration of the reactive species involved in the dissolution of UO_2 were considered to remain constant. Furthermore, since concentrations of catalytic species were expected to remain at a low level in solution, their impact on the dissolution rates was expected to be low. Nevertheless, their concentration were gradually increasing during this step due to the dissolution reaction [29]. Then, when their concentration reached about 10^{-3} mol.L^{-1}, the dissolution was accelerating significantly. Consequently, the dissolution rate was increasing continuously, leading to the establishment of the third dissolution step (catalysed domain). The relative mass losses ($\Delta m/m_0$ (wt. %)) and uranium concentration (C_U (mol.L^{-1})) obtained at the end of the induction period were varying with the dissolution conditions. As instance, uranium concentration ranged from 4.1×10^{-5} mol.L^{-1} in 2 mol.L^{-1} HNO_3 at room temperature to 5.7×10^{-4} mol.L^{-1} in 1 mol.L^{-1} HNO_3 at 60°C (**Table 4**). It is consistent with that obtained for pure UO_2 (from 9.6×10^{-5} mol.L^{-1} in 1 mol.L^{-1} HNO_3 at room temperature to 1.6×10^{-4} mol.L^{-1} in 1 mol.L^{-1} HNO_3 at 60°C). Since the presence of PGM led to an increase of the dissolution rate measured during the induction period, modifications in the dissolution mechanism of UO_2 were suspected in the presence the PGM bearing metallic particles.

3.3.2. Comparison with UO_2

In order to highlight the impact of PGM elements on the dissolution of UO_2 in nitric acid, the normalized dissolution rates ($R_{L.0}$ (U) (g.m^{-2}.d^{-1}) and the durations of the induction periods were compared to those determined for pure UO_2, used as reference material [20]. Such a comparison is given in **Figure 8** (0.1 mol.L^{-1}, room temperature) and in **Figure 9** (for all temperatures and nitric acid concentrations considered).

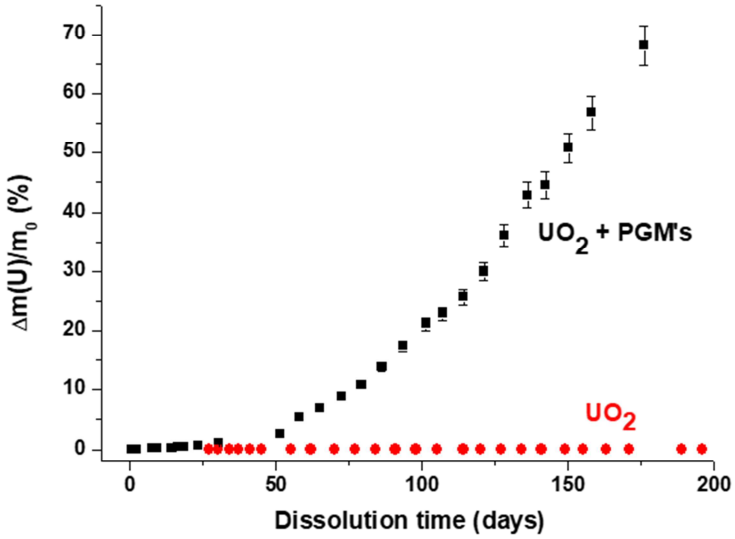

Figure 8. Evolution of the relative mass loss $\Delta m(U)/m_0$ obtained during the dissolution of sintered samples of UO_2 + 3 mol.% PGM and UO_2 (reference material) in 0.1 mol.L^{-1} HNO_3 and at room temperature.

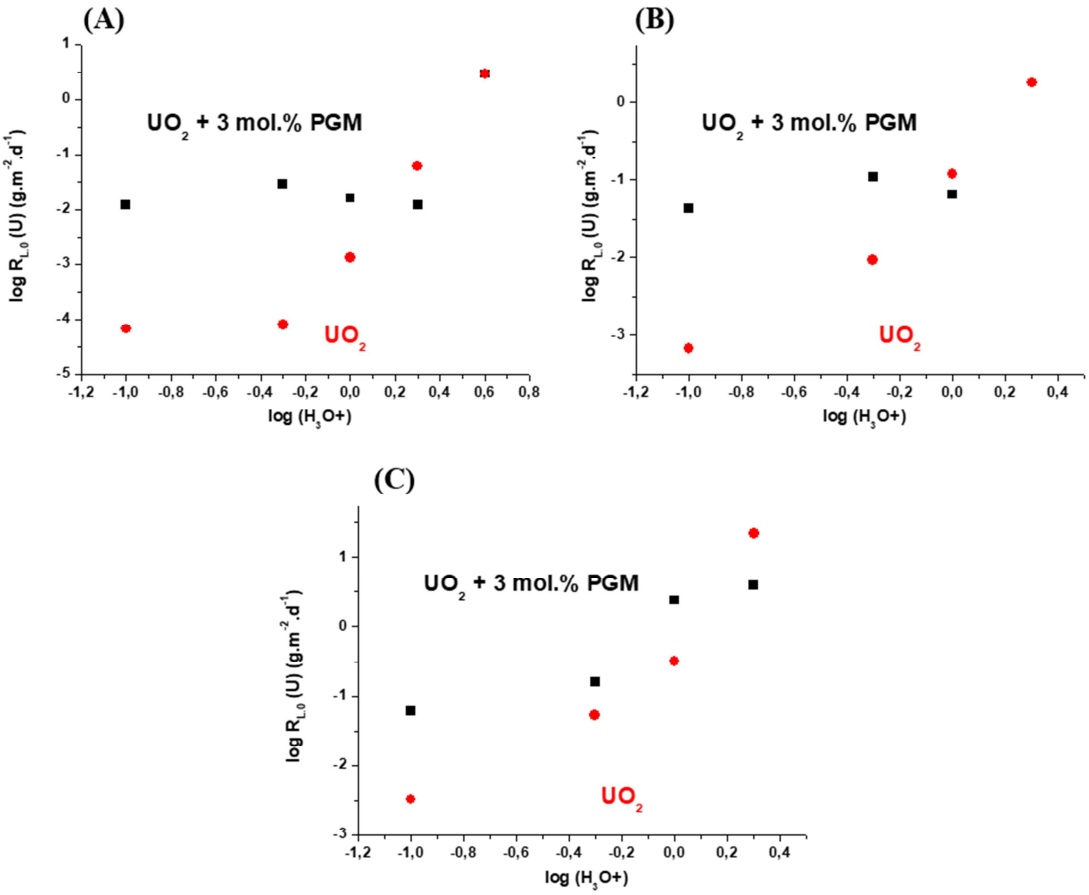

Figure 9. Variation of log $R_{L,0}$(U) versus log (H_3O^+) (proton activity) determined during the dissolution of UO_2 [20] and UO_2 + 3 mol.% PGM pellets in 0.1 mol.L^{-1}, 0.5 mol.L^{-1}, 1 mol.L^{-1}, 2 mol.L^{-1} and 4 mol.L^{-1} HNO_3 at room temperature (A), 40°C (B) and 60°C (C).

The results presented in both figures highlighted a very important effect due to the presence of the PGM as metallic particles for nitric acid concentrations lower than 1 mol.L^{-1}, which was amplified for lower temperatures. Indeed, this effect was found to be one to several orders of magnitude higher than that reported for tetravalent or trivalent elements. As instance, the normalized dissolution rate obtained in 0.1 mol.L^{-1} HNO_3 at room temperature for UO_2 + 3 mol.% PGM (i.e. (1.2 ± 0.2) × 10^{-2} g.m^{-2}.d^{-1}) was found to be 200 times higher than that reported pure UO_2 (i.e. $R_{L,0}$(U) = (6.7 ± 0.3) × 10^{-5} g.m^{-2}.d^{-1}). In the same conditions, the relative mass loss ($\Delta m/m_0$ (wt. %)) determined after 175 days of dissolution was increasing by a factor of 1800. In contrast, the difference observed was smaller in the more concentrated nitric acid solutions (typically in 2 mol.L^{-1} or 4 mol.L^{-1} HNO_3), to become almost inexistent in 4 mol.L^{-1} HNO_3 at room temperature ($R_{L,0}$(U) = 2.9 ± 0.2 g.m^{-2}.d^{-1}).

It is worth noting that the increase of the normalised dissolution rates $R_{L,0}$(U) obtained for UO_2 + 3 mol.% PGM was also associated to the strong decrease of the duration of the induction period, especially for low nitric acid concentrations (i.e. lower than 1 mol.L^{-1}). In order to underline this point, the ratio $t_{induction}(UO_2 + 3\ mol.\%\ PGM)/t_{induction}(UO_2)$ was plotted versus the HNO_3 concentration for the three temperatures considered (**Figure 10**). As instance, this ratio was found to 0.059 in 0.1 mol.L^{-1} HNO_3 at room temperature, as a consequence of the decrease of the steady state duration from 375 days (UO_2) to 22 days (UO_2 + 3 mol.% PGM) whereas it moved towards unit (i.e. 0.84) in 2 mol.L^{-1} HNO_3 at room temperature.

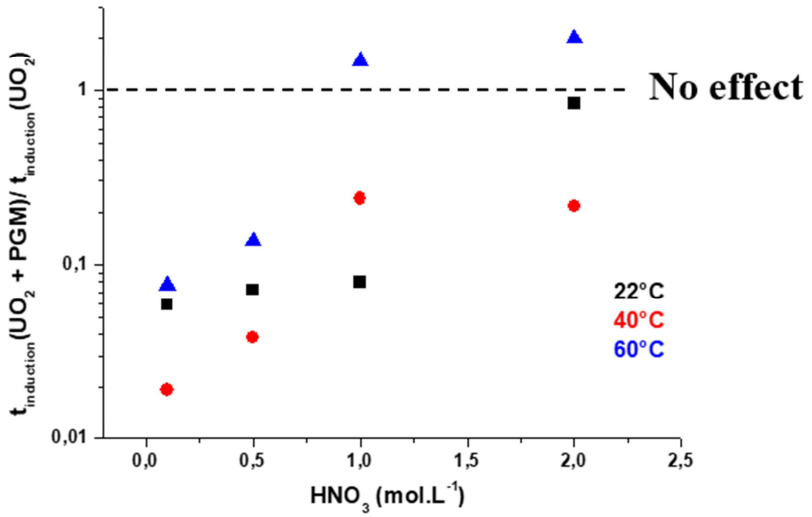

Figure 10. Variation of the $t_{induction}(UO_2 + 3\ mol.\%\ PGM)/t_{induction}(UO_2)$ ratio associated to steady state versus the concentration of nitric acid obtained during dissolution tests of UO_2 + 3 mol.% PGM and UO_2 (reference) sintered samples in 0.1 mol.L^{-1}, 0.5 mol.L^{-1}, 1 mol.L^{-1}, 2 mol.L^{-1} and 4 mol.L^{-1} HNO_3 at room temperature, 40°C and 60°C.

In order to underline any potential catalytic effect due to the presence of PGM elements on the dissolution of UO_2, the variation of Ln $R_{L,0}$ (U) obtained in 0.1 mol.L^{-1} HNO_3 was plotted versus the reciprocal temperature for UO_2 and UO_2 + 3 mol.% PGM sintered samples (**Figure 11**). From this representation, apparent activation energy of the overall dissolution reaction E_{app} was evaluated, as an important indicator of the predominant mechanism occurring during dissolution. Indeed, Lasaga *et al.* [30] showed that reactions which involve the breaking of strong bonds are associated to the highest activation energies (higher than 160 kJ.mol^{-1}). Typically, aqueous diffusion-controlled phenomena are characterized by activation energies lower than 20 kJ.mol^{-1} whereas minerals dissolving *via* surface controlled reactions are associated to E_{app} values between 40 to 90 kJ.mol^{-1}. Lasaga pointed out that the low activation energies associated to surface reaction-controlled mineral dissolution may reflect that chemisorption/desorption occurred prior to mineral dissolution. The E_{app} values associated to the dissolution of UO_2 + 3 mol.% PGM and UO_2 sintered samples in 0.1 mol.L^{-1} HNO_3 were found to 35 ± 12 kJ.mol^{-1} and 87 ± 8 kJ.mol^{-1}, respectively (**Figure 11**). They suggested the existence of surface-controlling phenomena for both materials. Moreover, the comparison of the two E_{app} values showed a decrease by a factor of 2.5 when PGM elements were present in the sample, which confirmed the important effect already mentioned. This clearly underlined the catalytic role of PGM elements during the dissolution of UO_2 in low concentrated nitric acid solution (such as 0.1 mol.L^{-1} HNO_3).

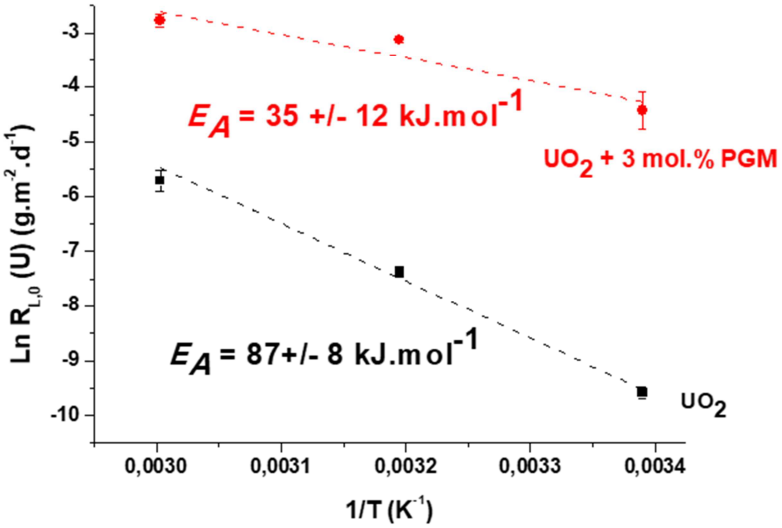

Figure 11. Variation of Ln $R_{L,0}$ (U) versus the reciprocal temperature obtained during the dissolution of UO_2 + 3 mol.% PGM and UO_2 (reference material) sintered samples in 0.1 mol.L^{-1} HNO_3. Continuous lines correspond to the obtained linear regression from experimental data.

Cordara *et al.*[20] already described that the dissolution mechanism of UO_2 moved from surface controlling reaction in the lower concentrated nitric acid solution (C_{HNO_3} < 1 mol.L^{-1}) to the oxidation of U(IV) in U(VI) by nitrate ions at the solid/solution interface for higher concentrations. This change

in the preponderant mechanism was confirmed for samples doped with PGM elements. Indeed, the variation of $R_{L,0}(UO_2+PGM)/R_{L,0}(UO_2)$ versus nitric acid concentration (**Figure 12**) confirmed the existence of a very important impact due to the presence PGM elements for C_{HNO_3} < 1 mol.L^{-1} and even more when the temperature was low. Based on the results obtained, this effect was directly associated to the catalytic role of PGM metallic particles. On the contrary, for higher nitric acid concentrations, the oxidation of U(IV) in U(VI) by nitrogen species became predominant, masking such catalytic phenomenon.

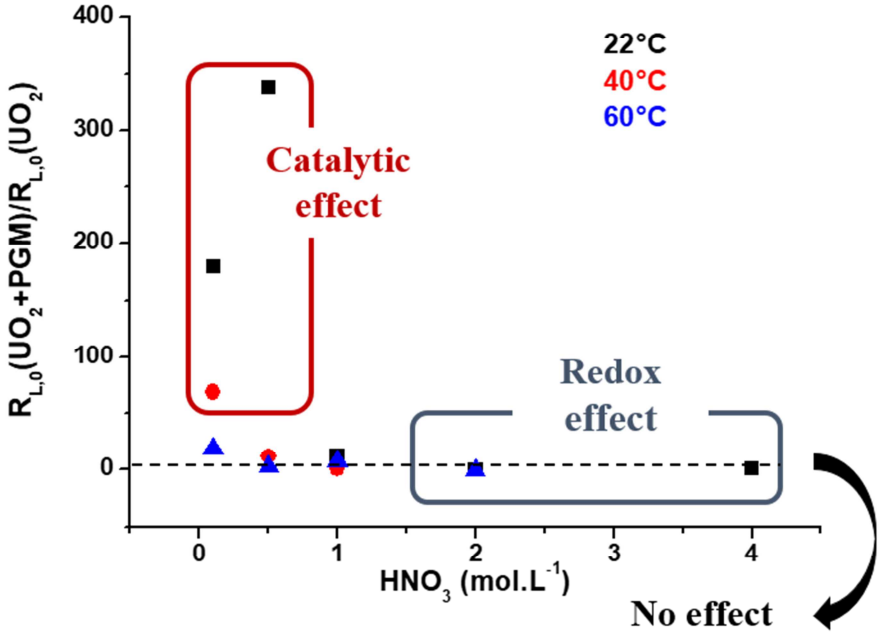

Figure 12. Variation of the $R_{L,0}(UO_2+PGM)/R_{L,0}(UO_2)$ ratio as a function of the nitric acid concentration during dissolution tests at various temperatures (RT, 40°C and 60°C).

3.3.3. Discrimination of PGM contributions

The impact of PGM elements could be explained in the light of two contributions. The first one could be associated to the development of redox reaction located at the metallic particles/UO_2/solution interface, leading to the reduction of nitrate ions into nitrogen oxide species. These latter could produce nitrous acid (HNO_2) and thus induce autocatalytic dissolution mechanism (according to equations 9-11) [29].

$$UO_2(s) + 2HNO_3(aq) + 2H^+ \rightarrow UO_2^{2+}(aq) + 2NO_2(aq) + 2H_2O \quad (9)$$

$$2NO_2(aq) + H_2O \leftrightharpoons HNO_2(aq) + HNO_3(aq) \quad (10)$$

$$UO_2(s) + 2HNO_2(aq) + 2H^+ \rightarrow UO_2^{2+}(aq) + 2NO(aq) + 2H_2O \quad (11)$$

The second contribution could result from the reduction of nitrate ions in solution, which could be catalysed by the presence of PGM metallic particles in solution. In order to evidence the role of both contributions on the overall dissolution process, complementary experiments were performed by using UO_2 sintered samples doped with one of the three PGM elements and by making dissolution tests with the addition of PGM metallic particles in solution. All these complementary dissolution tests were performed in 0.1 mol.L^{-1} HNO_3 at 60°C in order to enhance the impact of PGM bearing metallic particles, keeping unchanged all the other parameters associated to the dissolution protocol.

The results obtained during this series of experiments are gathered in **Figure 13** and in **Table 5**. They clearly evidenced the impact linked to the presence of PGM metallic particles in solution. Indeed, compared to the dissolution of UO_2 reference material ($R_{L.0}$ = (3.3 ± 0.1) × 10^{-3} g.m^{-2}.d^{-1}), the presence of rhodium or palladium metallic powder in solution induced an important increase of the normalized dissolution rate ($R_{L.0}$ = (2.3 ± 0.1) × 10^{-1} g.m^{-2}.d^{-1} for Rh and $R_{L.0}$ = (9.3 ± 0.2) × 10^{-2} g.m^{-2}.d^{-1} for Pd). For both elements, the existence of catalytic effect coming from the presence of metallic particles in the solution was clearly demonstrated in 0.1 mol.L^{-1} HNO_3 at 60°C. This very important impact was also associated to the decrease of the duration of the induction period from 120 days (for UO_2) to 22.9 and 2.3 – 3.0 days in the presence of powdered metallic rhodium and palladium, respectively (**Table 5**).

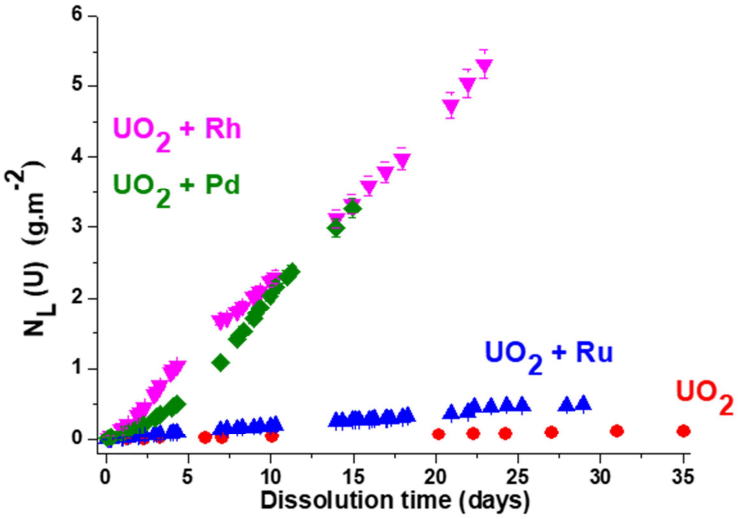

Figure 13. Evolution of the normalised weight losses N_L(U) obtained during the dissolution of UO_2 sintered pellets in 0.1 mol.L^{-1} HNO_3 at 60°C in the presence of PGM metallic powders in solution : Rh (▼), Pd (◆) and Ru (▲).

On the contrary, the impact observed in the presence of metallic ruthenium was lower than that observed for the two other PGM elements (**Figure 13**). This difference could be due to the properties

of the commercial metallic ruthenium powder used during the experiment. Indeed, this powder remained undissolved in HNO_3 contrarily to what was mentioned by several authors. For example, Swain *et al.* [31] reported that this element was mainly found in solution as Ru(II) or Ru(III) in nitric acid media, especially as ruthenium nitrosyl complexes $RuNO^{3+}$ with nitrate, nitrite or hydroxo ligands. Furthermore, according to Mousset [17], two-thirds of the ruthenium content was dissolved in boiling nitric acid during the SNF reprocessing and formed $RuNO^{3+}$ complexes with uranium, plutonium and fission products. The remaining ruthenium was found as undissolved metallic particles. One explanation for this phenomenon could find its origin from the formation of ruthenium oxide passivate layer at the solid/liquid interface. This assumption was confirmed by dissolution tests performed on the commercial metallic PGM powders in 0.1 $mol.L^{-1}$ HNO_3 at 60°C. Indeed, in these conditions, ruthenium was not dissolved (concentration under the detection limit obtained by ICP-AES) contrarily to what was observed for metallic palladium or rhodium powders. Furthermore, the oxidation of ruthenium metal was also studied in air by Sharma et al. The authors observed the formation of RuO_2 layer located at the surface of the ruthenium metallic powders [32].

The development of redox reactions between ε-particles and HNO_3 significantly affected the uranium release. For instance, in the presence of rhodium powder in solution, the normalised dissolution rate obtained in 0.1 $mol.L^{-1}$ HNO_3 and at 60°C was increased from $R_{L,0}$ (U) = (3.3 ± 0.1) × 10^{-3} $g.m^{-2}.d^{-1}$ (UO_2, reference material) to $R_{L,0}$ (U) = (2.3 ± 0.1) × 10^{-1} $g.m^{-2}.d^{-1}$ (**Table 5**).

The second contribution was evidenced through dissolution tests performed on UO_2 pellets doped with individual PGM. In this way, samples of UO_2 + 3 mol.% Ru, UO_2 + 3 mol.% Rh and UO_2 + 3 mol.% Pd were thus submitted to dissolution tests in 0.1 $mol.L^{-1}$ HNO_3 at 60°C (**Figure 14**). The associated normalised dissolution rates and induction period durations are summarized in **Table 5**. The normalised dissolution rates $R_{L,0}$ *(U)* determined for UO_2 + 3 mol.% Ru, UO_2 + 3 mol.% Rh and UO_2 + 3 mol.% Pd pellets reached (1.7 ± 0.1) × 10^{-1} $g.m^{-2}.d^{-1}$, (6.1 ± 0.1) × 10^{-2} $g.m^{-2}.d^{-1}$ and (3.2 ± 1.0) × 10^{-2} $g.m^{-2}.d^{-1}$, respectively. All these values were found to be higher than that determined for pure UO_2 in the same conditions (i.e. $R_{L.0}$ (U) = (3.3 ± 0.1) × 10^{-3} $g.m^{-2}.d^{-1)}$. Thanks to this comparison, it was also possible to sort the role of each element. Indeed, it appeared that the incorporation of ruthenium in UO_2 pellets was associated to the most important effect (factor of about 50 compared to 18 for palladium). Moreover, pondered normalized dissolution rate was evaluated considering the three values deduced from individual incorporation of each PGM as well as weight loadings of Rh, Pd and Ru in the samples. This average value reached (1.1 ± 0.6) × 10^{-1} $g.m^{-2}.d^{-1}$, which was consistent with that determined when incorporating simultaneously the three PGM ($R_{L,0}$ (U) = (6.3 ± 0.3) × 10^{-2} $g.m^{-2}.d^{-1}$). Thus, no synergistic effect was observed.

Table 5. Normalised dissolution rates $R_{L,0}$(U) (g.m^{-2}.d^{-1}) determined during the steady state step obtained during the dissolution of UO_2 + 3 mol.% PGM (mixed); UO_2 + 3 mol.% PGM (individual) and UO_2 + separated PGM powder in 0.1 mol.L^{-1} HNO_3 at 60°C.

	$R_{L.0}$ (U) (g.m^{-2}.d^{-1})	Steady state duration (days)
UO_2	$(3.3 \pm 0.1) \times 10^{-3}$	120
UO_2 + 3 mol.% PGM	$(6.2 \pm 0.3) \times 10^{-2}$	7.2 - 9.2
UO_2 + 3 mol.% Rh	$(6.1 \pm 0.1) \times 10^{-2}$	4.4 - 7.0
UO_2 + Rh powder	$(2.3 \pm 0.1) \times 10^{-1}$	22.9
UO_2 + 3 mol.% Pd	$(3.2 \pm 1.0) \times 10^{-2}$	14.9
UO_2 + Pd powder	$(9.3 \pm 0.2) \times 10^{-2}$	2.3 – 3.0
UO_2 + 3 mol.% Ru	$(1.7 \pm 0.1) \times 10^{-1}$	0.4 - 1.0
UO_2 + Ru powder	$(1.8 \pm 0.1) \times 10^{-2}$	28.9

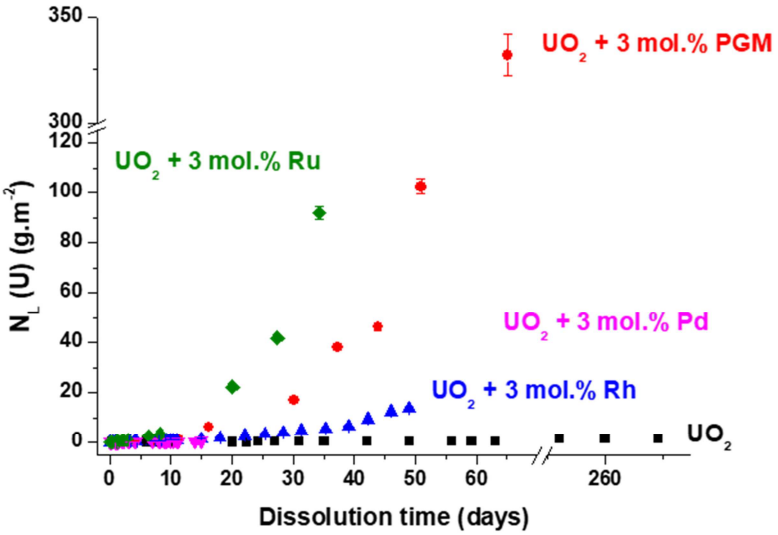

Figure 14. Evolution of the normalised weight losses N_L(U,t) obtained during the dissolution of UO_2 + 3 mol.% Rh, UO_2 + 3 mol.% Ru, UO_2 + 3 mol.% Pd pellets in 0.1 mol.L^{-1} HNO_3 at 60°C. The results obtained in the same conditions for UO_2 + 3 mol.% PGM and for UO_2 are reported as a comparison.

4. Insights in the understanding of UO_2 dissolution in the presence of PGM

All the results presented in this work evidenced the impact of PGM bearing metallic particles during UO_2 dissolution. This impact could evidently result from the incorporation of metallic particles in the UO_2 ceramics (which could lead to the presence of crystalline defects), from the modification of

UO_2 reactivity at the local scale and from the increase of oxidizing species regarding to U(IV) at the solid/liquid interface.

One of the assumptions supporting the strong increase of UO_2 dissolution rate in the presence of PGM is linked to the development of redox reactions between metallic particles and HNO_3, which could directly affect the oxidation of U(IV) at the solid/liquid interface. The dissolution of UO_2 in the presence of HNO_2 was often reported to be autocatalytic since both NO and NO_2, produced by redox reaction between U(IV) and HNO_2 (equation 11), recombine to finally form again HNO_2 according to equation 12 [6-9, 12, 29, 33, 34].

$$NO(aq) + NO_2(aq) + H_2O \leftrightharpoons 2\,HNO_2(aq) \quad (12)$$

Assuming that PGM bearing metallic particles could induce the reduction of HNO_3 to HNO_2, fast dissolution of UO_2 is then possible (equation 11). Consequently, the induction period can be associated to the slow dissolution of UO_2 associated to U(IV) oxidation by nitrate ions (E° (NO_3^-/HNO_2) = 0.934 V/NHE and E°(UO_2^{2+}/U^{4+}) = 0.327 V/NHE). When sufficient concentration of HNO_2 is reached in solution, autocatalytic reaction becomes preponderant. This assumption is supported by several papers reported in literature. For instance, Souza-Garcia *et al.*[35] studied the reduction of nitrate ions by modified Pt/Pd electrodes in H_2O and D_2O in the presence (or not) of KNO_3. They followed the reduction by voltammetry and FTIR spectroscopy. They observed the reduction of nitrate ions into NO, N_2O, NH_2OH, N_2 and NH_3. These species could lead to the formation of NO_2 or HNO_2 in HNO_3. Furthermore, Balbaud *et al.* [36] studied the reduction of HNO_3 for various initial concentrations. They reported the formation of NO for C_{HNO3} < 8 mol.L^{-1} and of NO_2 for higher concentrations. In order to explain the formation of these species, they proposed a mechanism involving the reduction of HNO_3 to HNO_2. Indeed, this reduction was also reported for long on the surface of Pt electrode [16, 37-39]. The nitrous acid thus produced would lead to the formation of NO and NO_2 by reduction with Pt. Since PGM elements have close properties compared to Pt, one can expect similar mechanism in this work.

Moreover, the analysis of the standard reduction potentials of platinum group metals, i.e. E° (Ru^{2+}/Ru) = 0.455 V/NHE, E° (Pd^{2+}/Pd) = 0.951 V/NHE, E° (Rh^{3+}/Rh) = 0.758 V/NHE and E° (Rh^{+}/Rh) = 0.600 V/NHE show that metallic PGM cannot directly oxidize tetravalent uranium to UO_2^{2+} (E° (UO_2^{2+}/U^{4+}) = 0.327 V/NHE). However, metallic ruthenium and rhodium are able to reduce nitrate ions to HNO_2 in nitric acid solutions (E° (NO_3^-/HNO_2) = 0.934 V/NHE). It is also the case for dissolved Ru^{2+} (E° (Ru^{3+}/ Ru^{2+}) = 0.249 V/NHE). Furthermore, Kim et al. [40] already reported redox reactions showing the reduction of NO_3^- to HNO_2 by Ru^{3+}, leading to the formation of tetravalent ruthenium.

Concerning the specific effect of palladium, even if this metal can not reduce directly nitrate ions as the other PGM, the dissolved Pd^{2+} can directly oxidize U^{4+} to UO_2^{2+}. It is worth noting that Ru

and Rh metal particles are partly and slowly dissolved in nitric acid [41] contrarily to palladium, which dissolution was reported to be rapid. To conclude, one can make the hypothesis that uranium oxidation occurring during the dissolution involves the initial reduction of nitrate to HNO_2 for metallic rhodium and ruthenium and direct oxidation of U^{4+} by Pd^{2+} for palladium.

In summary, one can propose that the dissolution of UO_2 in the presence of PGM would be linked to redox reaction between HNO_3 and ε metallic particles, leading to the reduction of nitrate ions to nitrogen oxides. This reduction reaction, which is proposed in step 1 in **Figure 15**, must be accompanied by the oxidation of the metallic particles from M^0 to M^{n+}. This oxidation could induce the formation of PGM oxides or free cations in solution. However as already discussed, the determination of the PGM concentrations in solution by ICP-AES was impossible because of interferences coming from the higher amount of uranium solubilized compared to PGM. After this first step, the production of NO_2(g) leads to the formation of nitrous acid in solution, by the NO_2 disproportionation reaction, which induces the fast dissolution of UO_2 due to its strong oxidative power regarding to U(IV). This would finally affect the release of uranium as UO_2^{2+} form (**Figure 15**). The proposed mechanism support the existence of autocatalytic reaction since HNO_2 is consumed in step 3 then produced again in step 2 due to recombination of nitrogen based species in solution. However, one can not fully exclude the existence of additional U(IV) oxidation reaction coming from the presence of PGM^{n+} in solution.

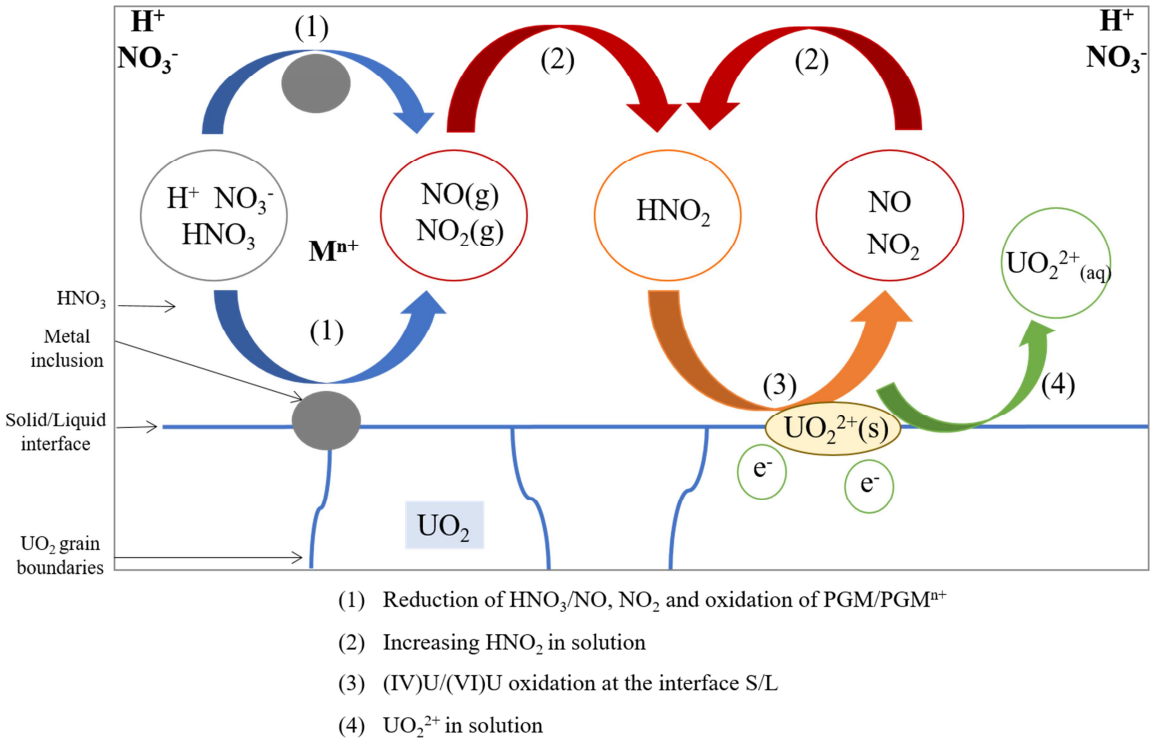

Figure 15. Proposed dissolution mechanism of UO_2 doped with PGM elements (ε particles) in nitric acid.

5. Conclusion

The effect of ε metallic particles containing PGM elements on the dissolution of sintered UO_2 samples was examined through the direct comparison of the results obtained during multiparametric dissolution tests of sintered UO_2 and UO_2 + 3mol.% PGM samples. This effect was found to be more important when the concentration of nitric acid was low (typically for $C_{HNO_3} < 1$ mol.L^{-1}). On the contrary, for nitric acid concentrations higher than 1 mol.L^{-1}, the effect of PGM elements was lowered due to the preponderant oxidation of U(IV) by nitrate ions. The effect of PGM elements was evidenced by the significant increase of the normalised dissolution rate along with the decrease of the duration of the induction period. Simultaneously, the decrease of the apparent activation energy associated to the reaction of dissolution supported the existence of catalytic effect. This latter was connected to redox reaction between the metallic particles and nitrate ions either in solution or at the PGM/UO_2/solution interface. Such reactions induced the formation of nitrogen species close to the PGM bearing ε particles. Among them, nitrous acid formed by reduction of nitrate ions at the metallic particles surface played an important role due to its strong oxidative power regarding to U(IV). The direct comparison of the results obtained for palladium, rhodium and ruthenium highlighted that the latter was associated to the stronger effect. Additionally, no synergistic effect was evidenced when mixing the three PGM elements.

To confirm and validate the UO_2 dissolution mechanism in presence of PGM metallic particles proposed in this work, further studies involving ICP-MS analyses followed by speciation calculations will be develop. Due to the important effect observed, the development of such redox reactions is expected to induce significant microstructural evolutions at the solid/liquid interface. In order to follow this impact, *operando* monitoring of the solid/liquid interface during dissolution tests in 0.1 and 1 mol.L^{-1} HNO_3 are now developed. It will allow not only to sort all the contributions coming from solution and solid/liquid interfaces but also to follow potential evolution of the UO_2 surface reactivity (associated to the existence of preferential dissolution zones) consequently to the accumulation of oxidizing species of U(IV) close to the particles/UO_2/solution.

References

[1] H. Kleykamp, The chemical state of the fission products in oxide fuels, J. Nucl. Mater. 131(2) (1985) 221-246.

[2] P.C. Burns, R.C. Ewing, A. Navrotsky, Nuclear Fuel in a Reactor Accident, Science 335(6073) (2012) 1184-1188.

[3] J. Bruno, R.C. Ewing, Spent nuclear fuel, Elements 2(6) (2006) 343-349.

[4] M.H.A. Piro, J. Banfield, K.T. Clarno, S. Simunovic, T.M. Besmann, B.J. Lewis, W.T. Thompson, Coupled thermochemical, isotopic evolution and heat transfer simulations in highly irradiated UO_2 nuclear fuel, J. Nucl. Mater. 441(1) (2013) 240-251.

[5] A. Vaudano, Monographie DEN, Le traitement-recyclage du combustible nucléaire usé. CEA Saclay et le Moniteur (Ed.), 2008.

[6] T. Fukasawa, Y. Ozawa, Relationship between dissolution rate of uranium dioxide pellets in nitric acid solutions and their porosity, Journal of Radioanalytical and Nuclear Chemistry 106(6) (1986) 345-356.

[7] T. Fukasawa, Y. Ozawa, F. Kawamura, Generation and decomposition behavior of nitrous-acid during dissolution of UO_2 pellets by nitric acid, Nuclear Technology 94(1) (1991) 108-113.

[8] Y. Ikeda, Y. Yasuike, Y. Takashima, Y.-Y. Park, Y. Asano, H. Tomiyasu, ^{17}O NMR study on dissolution reaction of UO_2 in nitric acid mechanism of lectron transfer, Journal of Nuclear Science and Technology 30(9) (1993) 962-964.

[9] Y. Ikeda, Y. Yasuike, K. Nishimura, S. Hasegawa, Y. Takashima, Kinetic-Study on Dissolution of UO_2 Powders in Nitric-Acid, J. Nucl. Mater. 224(3) (1995) 266-272.

[10] K. Nishimura, T. Chikazawa, S. Hasegawa, H. Tanaka, Y. Ikeda, Y. Yasuike, Y. Takashima, Effect of Nitrous-Acid on Dissolution of UO_2 Powders in Nitric-Acid Optimal Conditions for Dissolving UO_2, Journal of Nuclear Science and Technology 32(2) (1995) 157-159.

[11] M. Shabbir, R.G. Robins, Kinetics of the dissolution of uranium dioxide in nitric acid. I, Journal of Applied Chemistry 18(5) (1968) 129-134.

[12] R.F. Taylor, E.W. Sharratt, L.E.M. De Chazal, D.H. Logsdail, Dissolution rates of uranium dioxide sintered pellets in nitric acid systems, Journal of Applied Chemistry 13(1) (1963) 32-40.

[13] M.R. Shabbir, R. G. , The effect of crystallographic orientation on the dissolution of uranium dioxide in nitric acid, J. Nucl. Mater. 25(2) (1968) 236-237.

[14] J.P. Glatz, H. Bokelund, S. Zierfuß, Analysis of the Off-Gas from Dissolution of Nuclear Oxideand Carbide Fuels in Nitric Acid, Radiochimica Acta, 1990, p. 17.

[15] Y. Zhao, J. Chen, Studies on the dissolution kinetics of ceramic uranium dioxide particles in nitric acid by microwave heating, J. Nucl. Mater. 373(1) (2008) 53-58.

[16] K.G. Schmid G., Berichte der Bunsengesellschaft für physikalische Chemie 68(7) (1964) 677-688.

[17] M. F., Electro-volatilisation du ruthénium en milieu nitrique. -Influences de la nature des formes chimiques du ruthénium et de la composition des solutions modèles de

dissolution, PhD, University Pierre et Marie Curie, Paris VI, , University of Pierre et Marie Curie, Paris VI, 2004.

[18] Y. Ikeda, Y. Yasuike, Y. Takashima, K. Nishimura, S. Hasegawa, Acceleration Effect of Noble Metals on Dissolution Rate of UO_2 Powders in Nitric Acid, Journal of Nuclear Science and Technology 30(5) (1993) 485-487.

[19] P.T. C. Poinssot, J-P.Grouiller, J. Pavageau, J-P. Piron, M. Pelletier, P. Dehaudt, C. Cappelaere, R. Limon, L. Desgranges, C. Jegou, C. Corbel, S. Maillard, M-H. Faure, J-C. Cicariello, M. Masson, CEA DEN Rapport PRECCI, in: CEA (Ed.) 2001, p. 130.

[20] T. Cordara, S. Szenknect, L. Claparede, R. Podor, A. Mesbah, C. Lavalette, N. Dacheux, Kinetics of dissolution of UO_2 in nitric acid solutions: A multiparametric study of the non-catalysed reaction, J. Nucl. Mater. 496 (2017) 251-264.

[21] J. Martinez, N. Clavier, A. Mesbah, F. Audubert, X.F. Le Goff, N. Vigier, N. Dacheux, An original precipitation route toward the preparation and the sintering of highly reactive uranium cerium dioxide powders, J. Nucl. Mater. 462 (2015) 173-181.

[22] L.W. Finger, D.E. Cox, A.P. Jephcoat, A correction for powder diffraction peak asymmetry due to axial divergence, Journal of Applied Crystallography 27(6) (1994) 892-900.

[23] D. Horlait, L. Claparede, F. Tocino, N. Clavier, J. Ravaux, S. Szenknect, R. Podor, N. Dacheux, Environmental SEM monitoring of $Ce_{1-x}Ln_xO_{2-x/2}$ mixed-oxide microstructural evolution during dissolution, Journal of Materials Chemistry A 2(15) (2014) 5193-5203.

[24] F. Tocino, Contrôle microstructural des réactions rédox à l'interface solide/solution lors de la dissolution d'oxydes mixtes à base d'uranium (IV), Thèse Université de Montpellier, ICSM, (2015).

[25] A.C. Lasaga, Chemical-Kinetics of Water-Rock Interactions, Journal of Geophysical Research 89 (1984) 4009-4025.

[26] D. Langmuir, Aqueous environmental geochemistry,Printice Hall Inc, 1997.

[27] L. Desgranges, G. Baldinozzi, G. Rousseau, J.-C. Nièpce, G. Calvarin, Neutron Diffraction Study of the in Situ Oxidation of UO_2, Inorganic Chemistry 48(16) (2009) 7585-7592.

[28] N. J., Monographie DEN, Les combustibles nucléaires. CEA Saclay et Le Moniteur (Ed.) CEA(2009).

[29] T. Dalger, S. Szenknect, F. Tocino, L. Claparede, A. Mesbah, P. Moisy, N. Dacheux, Kinetics of dissolution of $Th_{0.25}U_{0.75}O_2$ sintered pellets in various acidic conditions, J. Nucl. Mater. 510 (2018) 109-122.

[30] A.C.K. Lasaga, R. J., Kinetics of geochemical processes, (1981).

[31] P. Swain, C. Mallika, R. Srinivasan, U.K. Mudali, R. Natarajan, Separation and recovery of ruthenium: a review, Journal of Radioanalytical and Nuclear Chemistry 298(2) (2013) 781-796.

[32] S. Sharma, L. Hines, Oxidation of Ruthenium, IEEE Transactions on Components, Hybrids, and Manufacturing Technology 6(1) (1983) 89-92.

[33] P. Marc, A. Magnaldo, A. Vaudano, T. Delahaye, É. Schaer, Dissolution of uranium dioxide in nitric acid media: what do we know?, EPJ N - Nuclear Sciences & Technologies 3(13) (2017) 1-13.

[34] D. Sicsic, Modélisation thermodynamique et cinétique de la réduction de l'acide nitrique concentré, PhD, University Pierre & Marie Curie, (2011).

[35] J. Souza-Garcia, E.A. Ticianelli, V. Climent, J.M. Feliu, Mechanistic changes observed in heavy water for nitrate reduction reaction on palladium-modified Pt(hkl) electrodes, Chemical Science 3(10) (2012) 3063-3070.

[36] F. Balbaud, G. Sanchez, G. Santarini, G. Picard, Cathodic Reactions Involved in Corrosion Processes Occurring in Concentrated Nitric Acid at 100 °C, European Journal of Inorganic Chemistry 2000(4) (2000) 665-674.

[37] K.J. Vetter, Entgegnung auf die vorstehende arbeit von schmid,g. Uber die autokatalytische natur der kathodischen reduktion von salpetersaure zu salpetriger saure, Z. Elektrochem. 63(9-10) (1959) 1189-1191.

[38] G. Schmid, M.A. Lobeck, Das Verhalten von salpetriger Säure und Salpetersäure an der rotierenden Scheibenelektrode. I. HNO_2 in schwefelsauren Lösungen ohne HNO_3-Zusatz, Berichte der Bunsengesellschaft für physikalische Chemie 73(2) (1969) 189-199.

[39] V.P. Razygraev, M.V. Lebedeva, S.A. Kabakchi, E.Y. Ponomareva, R.S. Balovneva, L.P. Lobanova, Features of cathode reduction of boiling solutions of nitric-acid on a platinum-electrode, Journal of Applied Chemistry of the Ussr 61(1) (1988) 67-73.

[40] E.-H. Kim, D.-S. Hwang, W.-M. Choung, J.-H. Park, J.-H. Yoo, C.-S. Choi, Dissolution of UO_2 by Photochemical Reaction, Radiochimica Acta, 1998, p. 147.

[41] T. Matsui, M. Ohkawa, R. Sasaki, K. Naito, Dissolution of the simulated fission-produced Mo,Ru,Rh,Pd alloys in boiling nitric acid solution, J. Nucl. Mater. 200(1) (1993) 11-15.